

# Sheets, filaments and clumps - high resolution simulations of how the thermal instability can form molecular clouds

C. J. Wareing<sup>1</sup>\*, S. A. E. G. Falle<sup>2</sup> and J. M. Pittard<sup>1</sup>

<sup>1</sup>*School of Physics and Astronomy, University of Leeds, Leeds, LS2 9JT, U.K.*

<sup>2</sup>*School of Mathematics, University of Leeds, Leeds, LS2 9JT, U.K.*

Accepted xxx. Received xxx; in original form xxx

## ABSTRACT

The hydrodynamic version of the adaptive mesh refinement (AMR) code, MG, has been employed to perform 3D simulations of the formation of collapsing cold clumps on the scale of a few parsecs, inside a larger cloud complex. The diffuse atomic initial condition consists of a stationary, thermally unstable, 200 pc diameter spherical cloud in pressure equilibrium with low density surroundings. The diffuse atomic cloud was seeded with 10% density perturbations at the finest initial grid level (0.29 pc) around  $n_H = 1.1 \text{ cm}^{-3}$  and evolved with self-gravity included from the outset. No magnetic field was imposed. Resimulation of a region of this simulation at higher resolution (down to 0.039 pc), shows that the thermal instability dynamically forms sheets and filaments. The natural width of the filaments is 0.1–0.3 pc. Following this, clumps grow at the intersections of filaments with size-scales of around 5 pc and aspect ratios around unity. Imposed on the entire potential well of the cloud, the FellWalker routine finds 21 distinct clumps. The properties of these clumps are in agreement with clumps observed in molecular clouds. Given their positions, at the interconnections of the filamentary network, many show evidence of infalling linear structure. Not all are gravitationally bound, but the convergent nature of the infall and increasing central density in each suggest they are highly-likely to form stars. Further simulation of the most massive clump reveals the final gravitational collapse of the clump, to resolved levels of density six orders of magnitude higher than the initial condition (i.e. to  $n_H > 10^6 \text{ cm}^{-3}$ ). The clumps within the cloud provide a realistic initial condition that can be used to study feedback in 1) individual clumps, 2) interacting clumps and 3) across the entire molecular cloud complex. Future work will consider the effects of cluster feedback in each of these three scenarios.

**Key words:** instabilities – ISM: structure – ISM: clouds – ISM: molecules – stars: formation – methods: numerical

## 1 INTRODUCTION

Extensive studies of the nearest star-forming clouds, most recently with the *Herschel* Space Observatory have revealed that every interstellar cloud contains an intricate network of interconnecting filamentary structures (see, for example, Section 2 of the review of André et al. (2014) and references therein). The data, from *Herschel* and near-IR studies for example, suggest a scenario in which these ubiquitous filaments represent a key step in the star formation process: large-scale flows compress the diffuse ISM and form molecular clouds; an interconnecting filamentary structure forms within these clouds; magnetic fields affect the flow of material and hence overall structure, although do not appear to

set the central densities in the filaments; gravity plays an increasingly important role, fragmenting the filaments once they are cold and dense into prestellar cores and finally protostars, commonly occurring at the intersections or hubs of the intricate structure.

Observational results now connect well with numerical simulations, as highlighted in Section 5 of André et al. (2014) and references therein. Early numerical simulations showed that gas is rapidly compressed into a hierarchy of sheets and filaments, without the aid of gravity (Bastien 1983; Porter, Pouquet & Woodward 1994; Vázquez-Semadini 1994; Padoan et al. 2001). Turbulent box simulations and colliding flows produce filaments (e.g. Mac Low & Klessen 2004; Hennebelle et al. 2008; Federrath et al. 2010; Gómez & Vázquez-Semadini 2014; Moeckel & Burkert 2015; Smith, Glover & Klessen 2014; Kirk et al. 2015). Hennebelle

\* E-mail: C.J.Wareing@leeds.ac.uk

& André (2013) demonstrated the formation of filaments through the velocity shear that is common in magnetised turbulent media. Other authors have explained filaments as the stagnation regions in turbulent media (Padoan et al. 2001). The formation of filaments preferentially perpendicular to the magnetic field lines is possible in strongly magnetised clouds (Li et al. 2010; Wareing et al. 2016). André et al. (2014) note that the same 0.1 pc filament width is measured for low-density, subcritical filaments suggesting that this characteristic scale is set by the physical processes producing the filamentary structure. Furthermore, they note that at least in the case of diffuse gravitationally unbound clouds (e.g. Polaris), gravity is unlikely to be involved. Large-scale compression flows, turbulent or otherwise, provide a potential mechanism, but it is not clear why any of these would produce filaments with a constant radius.

Smith, Glover & Klessen (2014) examined the influence of different types of turbulence, keeping the initial mean density constant in simulations without magnetic fields. They found that when fitted with a Plummer-like profile, the simulated filaments are in excellent agreement with observations, with  $p \approx 2.2$ , without the need for magnetic support. They found an average FWHM of  $\approx 0.3$  pc, when considering regions up to 1 pc from the filament centre, in agreement with predictions for accreting filaments. Constructing the fit using only the inner regions, as in *Herschel* observations, they found a resulting FWHM of  $\approx 0.2$  pc.

Kirk et al. (2015) used the FLASH hydrodynamics code to perform numerical simulations of turbulent cluster-forming regions, varying density and magnetic field. They used HD and MHD simulations, initialised with a supersonic ( $M \approx 6$ ) and super-Alfvénic ( $M_A \approx 2$ ) turbulent velocity field, chosen to match observations, and identified filaments in the resulting column density maps. They found magnetic fields have a strong influence on the filamentary structure, tending to produce wider, less centrally peaked and more slowly evolving filaments than in the hydrodynamic case. They also found the magnetic field is able to suppress the fragmentation of cores, perhaps somewhat surprisingly with super-Alfvénic motion involved in the initial condition. Overall, they noted the filaments formed in their simulations have properties consistent with the observations they set out to reproduce, in terms of radial column density profile, central density and inner flat radius.

Numerical simulations now include the thermodynamic behaviour of the cloud material, magnetic fields, gravity and feedback from massive stars, both radiative and dynamic (Beuther, Linz & Henning 2008; Harper-Clark & Murray 2009; Krumholz & Matzner 2009; Gray & Scannapieco 2011; Koenig et al. 2012; Rogers & Pittard 2013, 2014; Gatto et al. 2015; Offner & Arce 2015; Walch & Naab 2015; Walch et al. 2015; Girichidis et al. 2015; Körtgen et al. 2016). Supersonic, trans-Alfvénic turbulence has emerged as an ingredient which can, when injected at the right scale, result in the formation of filaments which possess properties remarkably similar to those derived from observational results whilst also reproducing the observed relatively smooth nature of the magnetic field. The interested reader is referred to lengthy introductions and reviews in the first sections of previous works by the same authors (Wareing et al. 2016, 2017a,b, 2018).

The work presented here continues the exploration of

the formation of clumps connected by filamentary structures through the use of hydrodynamic simulations of the thermal instability (TI) (Parker 1953; Field 1965). A number of authors have investigated analytically the effects of different mechanisms on the TI (Birk 2000; Nejad-Asghar & Ghanbari 2003; Stiele, Lesch & Heitsch 2006; Fukue & Kamaya 2007; Shadmehri 2009). Other groups have numerically investigated flow-driven molecular cloud formation including the effects of the TI (e.g. Lim, Falle & Hartquist 2005; Vázquez-Semadini et al. 2007; Hennebelle et al. 2008; Heitsch, Stone & Hartmann 2009; Ostriker, McKee & Leroy 2010; Van Loo, Falle & Hartquist 2010; Inoue & Inutsuka 2012). Hennebelle & Audit (2007) and Hennebelle et al. (2007) showed that HI clouds formed by thermal instability can explain a variety of observational characteristics. Inoue & Inutsuka (2012) used 3D MHD simulations, including radiative cooling and heating, to investigate the formation of molecular clouds. They consider the scenario of accretion of HI clouds and the piling up of the initial HI medium behind shock waves induced by accretion flows in order to form a molecular cloud. They find the resulting timescale of molecular cloud formation of  $\sim 10$  Myr is consistent with the evolutionary timescale of the molecular clouds in the LMC (Kawamura et al. 2009). This numerical work has included magnetic fields, self-gravity and the TI and has identified the thermal and dynamical instabilities that are responsible for the rapid fragmentation of the nascent cloud, largely through flow-driven scenarios.

Here we concentrate on the TI itself without any initial flow in a low-density cloud of quiescent diffuse medium initially in the unstable phase. The cloud is in pressure equilibrium with its lower-density (thus temperature above equilibrium) surroundings and we include accurate thermodynamics and self-gravity. In particular, the aim is to discern whether thermal instability alone can create high enough density structure that gravity can then dominate and drive the eventual collapse of the clump to form clusters of stars, regardless of the apparent status of the energy budget. This has not been observed in our previous works. Subsequent aims are to confirm whether such clumps display realistic properties when compared to observationally-derived properties, and whether mergers and collisions of clumps reproduce observations. The simulations presented herein are also intended as a means to define realistic initial conditions for cluster feedback simulations. In the next section the initial condition for this high resolution study is described. In Section 3, the numerical method and model are discussed. Results are presented and discussed in Section 4 with comparison to observation, before the work is concluded in Section 5, which also sets out how details of the simulations may be used in future works.

## 2 INITIAL CONDITIONS

Our recent work (Wareing et al. 2016, 2017a,b, 2018) has highlighted the way that the thermal instability (Field 1965), under the influence of gravity and realistic magnetic fields (magnetic pressure) in the ideal magnetohydrodynamic (MHD) limit, can drive the evolution of diffuse thermally unstable warm clouds from a pressure-supported quiescent low-density state to form high-density, cold ( $\leq 100$  K) clumps and, in the presence of magnetic field, sheet-like

structures that are filamentary in appearance, perpendicular to the applied field (Wareing et al. 2016, hereafter Paper I). The winds and ionising radiation from the massive stars that form through gravitational collapse of condensed molecular fragments in these sheets then strongly affect the environment into which core-collapse supernovae subsequently explode. Often not accounted for, this pre-supernovae feedback is particularly important to consider as high mass stars can introduce similar amounts of mass and energy to supernovae, and can significantly alter the evolution of the resulting supernova remnants (Wareing et al. 2017a,b, hereafter Papers II and III respectively).

In Paper II, separate simulations investigated realistic stellar wind feedback from a  $15 M_{\odot}$  star and a  $40 M_{\odot}$  star in the same  $17,000 M_{\odot}$  corrugated sheet-like molecular cloud influenced by magnetic field. The  $40 M_{\odot}$  star was able to evacuate a small central hole in the sheet whilst the majority of stellar wind material was channelled away by the magnetic field perpendicular to the sheet-like structure. Sub-sonic, sub-Alvénic motions along the field lines in the initial diffuse cloud had led to the formation of the corrugated sheet, even in this case of initial thermal and magnetic pressure equivalence ( $\beta_{\text{plasma}} = 1.0$ ). In Paper III, separate simulations investigated realistic stellar wind feedback from stars of mass  $15 M_{\odot}$ ,  $40 M_{\odot}$ ,  $60 M_{\odot}$  and  $120 M_{\odot}$  into the non-magnetic spherical cloud containing multiple clump-like cold condensations. There, feedback expanded symmetrically away from the point of injection until surrounding cloud structure inhibited and/or channelled the expansion, according to the way the dense structure in the spherical hydrodynamic cloud had formed under the influence of the thermal instability.

In our most recent work (Wareing et al. 2018, hereafter Paper IV), the model of stellar wind feedback in a sheet-like structure was applied to the Rosette Nebula, demonstrating that even in a cloud that resulted from an initial condition with twice the diameter and eight times more mass in the diffuse atomic cloud than that simulated in Paper II, a  $40 M_{\odot}$  star (similar to the dominant star in the Rosette Nebula) can still create a small hole in the centre of the sheet and launch focussed stellar wind flows perpendicularly away from the sheet. This model provided solutions to outstanding issues such as the age of the nebula, the small size of the central cavity, and the inferred-to-be missing stellar wind highlighted by Bruhweiler et al. (2010).

The range of simulations in Paper IV explored both hydrodynamic (HD) and MHD initial conditions. In this work, an early-stage central region of Paper IV Simulation 1, the HD simulation, has been extracted and placed in ambient pressure-matched surroundings. It has then been evolved at higher resolution in order to study the cloud complex formed and to determine the nature of the clumps therein. The aim is to explore how gravity takes over from the effect of thermal instability, without the extra complexity of magnetic field at this stage. If thermal instability subsequently dominated by gravity is able to create truly star-forming collapsing clumps with realistic properties, then a particularly simple scenario for the formation of stars is presented. Simulations in a future work will examine the role of magnetic field in the formation of cloud complexes and collapsing molecular substructure.

Condensations due to the thermal instability begin to

grow in the 200 pc diameter HD diffuse cloud initialised in Paper IV after 16 Myrs of evolved simulation time. At this time, their densities range up to  $n_H = 1.5 \text{ cm}^{-3}$ , unstable but very well-resolved and significantly above the initial diffuse level of  $n_H = 1.1 \text{ cm}^{-3} \pm 10\%$ . After this time, higher density structure grows in the Paper IV simulation and so  $t=16$  Myrs is the time at which the central region of the cloud is extracted for higher resolution investigation. The average pressure across the cloud at this time has decreased from the initial pressure of  $P_{\text{eq}}/k = 4700 \pm 300 \text{ K cm}^{-3}$  (set according to the heating and cooling equilibrium) to levels around  $P/k = 3800 \pm 200 \text{ K cm}^{-3}$ . This is driving a compression of the cloud by the surrounding medium in the Paper IV simulation. Isolating the study of the thermal instability from this effect is the secondary reason, after allowing for higher resolution, for extracting the 25 pc-radius sphere centred on  $(0,0,0)$ .

A slice through the centre of the new domain, containing the extracted section within  $r \leq 0.5$  (25 pc) is shown in Fig 1. The new domain extends to -1 and +1 (-50 pc to +50 pc) in all three Cartesian directions. The pressure and hence density outside the extracted region is defined by matching the average pressure across the central region to the equivalent stable equilibrium state density of  $n_H = 0.643 \text{ cm}^{-3}$  with the same pressure. The pressure-equivalent stable and unstable states are explicitly indicated in Fig 2. The surrounding medium is uniform and stationary. The total mass in the entire domain is approximately  $20,000 M_{\odot}$ , of which  $2800 M_{\odot}$  is in the extracted region,  $r \leq 0.5$ . Note from Fig 1 that the narrow density range results in equally narrow ranges of pressure and temperature. Extracting a spherical volume from a larger simulation in this way results in the edge of the volume cutting through some structure, but the range of density and pressure is low enough that this has little effect. The gravitational potential is also smoothly symmetric and relatively shallow. It is against this potential background of the developing cloud complex that deep localised wells should form, if the subsequent clumps in the complex undergo gravitational collapse. It is also useful to consider the other stable density matching this pressure, specifically  $n_H \approx 100 \text{ cm}^{-3}$ , as indicated in Fig 2. Assuming no change in pressure, this is the highest density that can be achieved by thermal instability alone in this choice of heating and cooling techniques and parameters. In reality, pressure changes also occur, but this provides a first order estimate in monitoring when gravity begins to become important: densities above this level indicates gravity taking over from the thermal instability.

### 3 NUMERICAL METHODS AND MODEL

The MG code has been used here in the same manner as throughout Papers I to IV. It is an upwind, conservative shock-capturing scheme employing multiple processors through parallelisation with the message passing interface (MPI) library. Integration in time proceeds according to Falle (1991) using a second-order accurate Godunov method (Godunov 1959) with a Kurganov Tadmor (Kurganov & Tadmor 2000) Riemann solver. Self-gravity is computed using a full-approximation multigrid to solve the Poisson equation. The same hierarchical AMR method (Falle 2005; Hub-

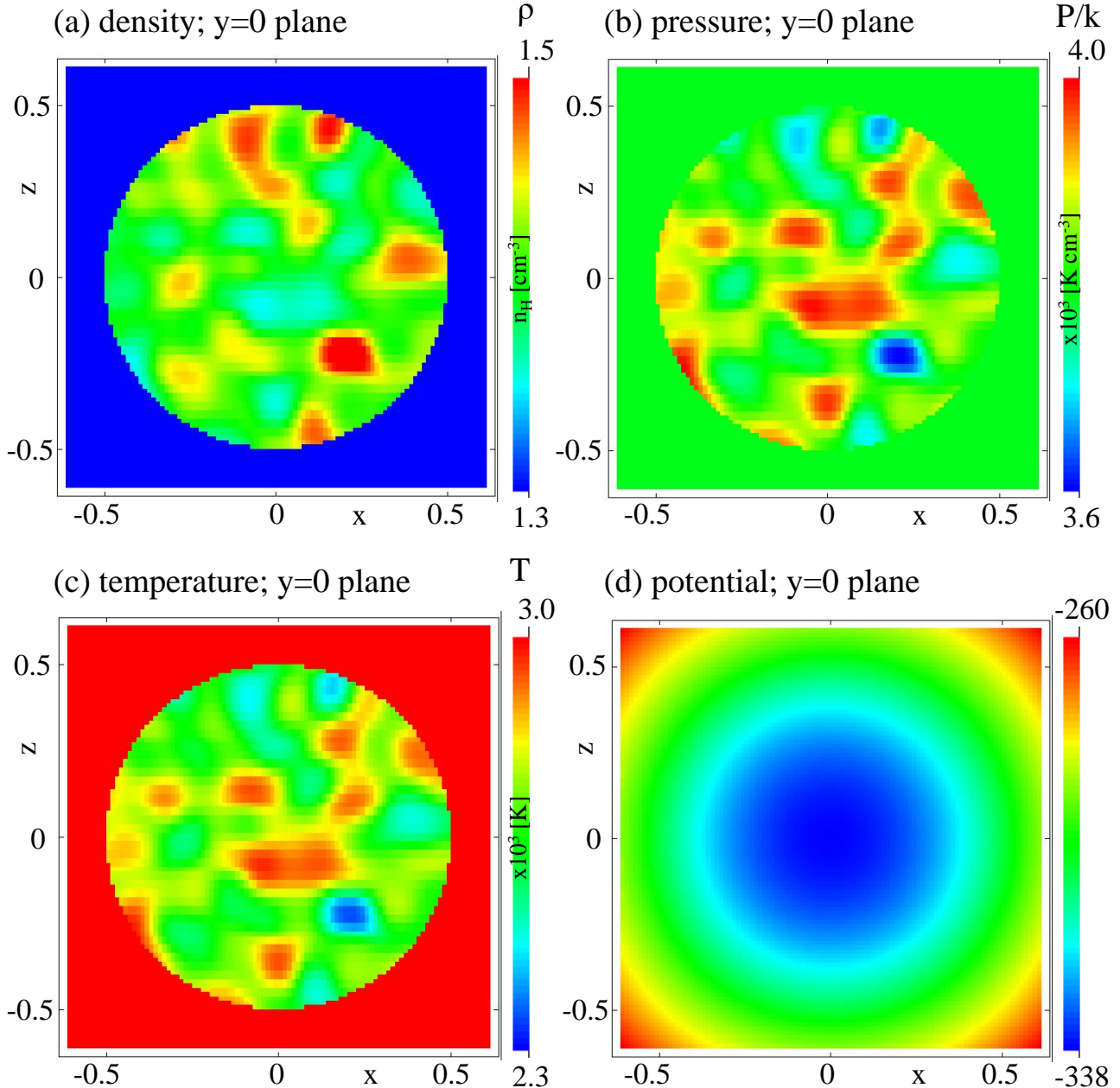


**Figure 1.** Initial conditions. The appearance of the extracted region of the Paper IV HD model on the  $y = 0$  plane, surrounded by the ambient pressure-matched stable conditions. The unit of distance is 50 pc. Raw data is available from <https://doi.org/10.5518/483> (for review purposes see <http://archive.researchdata.leeds.ac.uk/470/>).

number, Falle & Goodwin 2013) is employed on an unstructured grid. Free-flow boundary conditions were imposed on all boundaries. For more details, please consult previous works and Paper I in particular.

The 3D Cartesian  $xyz$  HD simulation in Paper IV employed 8 levels of AMR, with  $8 \times 8 \times 8$  cells on the coarsest G0 grid over a domain 300 pc on a side, making the finest grid resolution available 0.29 pc on G7. G0 needed to be coarse to ensure fast convergence of the MG Poisson solver. The Model 1 simulation herein defined  $10 \times 10 \times 10$  cells on the coarsest G0 level and 5 further levels of AMR. Mapping of the data from the Paper IV simulation onto the Model 1

simulation was performed in a simple linear fashion over all three coordinate directions for every cell in question. The diffuse structure in this grid was well-resolved (by 10 or more cells) in order to ensure no loss of detail, as can be seen in Fig. 1. The Model 1 simulation has approximately the same finest physical resolution as the original HD simulation from Paper IV. As the Model 1 simulation evolved, sharper, higher density features formed. To better resolve these features new simulations with an additional 1 or 2 levels of AMR were started from these times (Models 2 and 3, respectively). The Model 3 simulation would have  $1280^3$  cells on its finest level if it were fully resolved. A higher resolu-

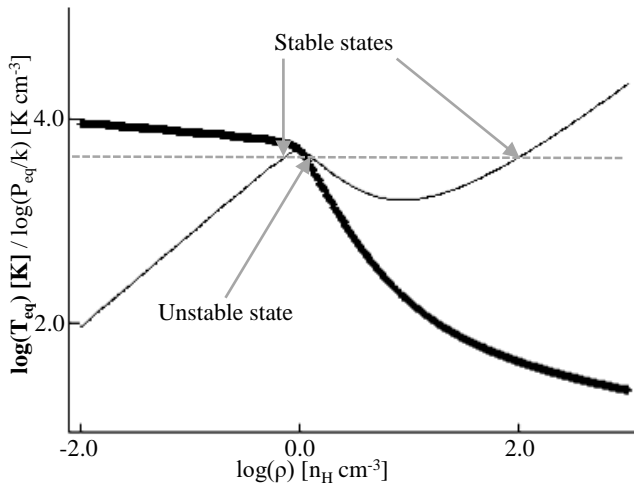


**Figure 2.** Equilibrium curves. Thermal equilibrium pressure ( $P_{eq}/k$  - thin line) and temperature ( $T_{eq}$  - thick line) vs. density for the cooling and heating functions selected in this work. Where the grey dashed line intersects the pressure curve (thin black line) indicates, from left to right, the stable, unstable and stable equilibrium states. Raw data is available from <https://doi.org/10.5518/483> (for review purposes see <http://archive.researchdata.leeds.ac.uk/470/>).

tion Model 4 simulation added a 9th level of AMR to resolve structure at 0.039 pc, but this was only briefly used due to the high computational cost. The simulations were either increased in resolution from an earlier stage, or stopped, when the maximum densities no longer met the Truelove criterion (Truelove et al. 1997). Finally, to examine the final evolution of the most massive clump, a further resimulation extracted the  $0.2^3$  region ( $10 \times 10 \times 10$  pc) containing this clump and resimulated it at a resolution of 0.016 pc in order to investigate gravitational collapse of this individual clump. The simulations were typically run across 96 cores of the ARC2-MHD DiRAC1 HPC facility at the University of Leeds (see also the Acknowledgments) and used in excess of 100,000 CPUhours.

The same heating and cooling prescriptions from Papers I to IV were employed, which are now summarised in brief. A constant heating factor of  $\Gamma = 2 \times 10^{-26}$  erg s $^{-1}$  was used, with the heating rate equal to  $\Gamma \rho$ . For low-temperature cooling ( $\leq 10^4$  K), the detailed prescription of Koyama & Inutsuka (2000), fitted by Koyama & Inutsuka (2002), and corrected according to Vázquez-Semadini et al. (2007) was used. At temperatures above  $10^4$  K the CLOUDY 10.00 prescription of Gnat & Ferland (2012) was used. These choices have enabled the definition of cooling rates over the temperature range from 10 K to  $10^8$  K - the range required by subsequent feedback simulations. The complete cooling prescription has been efficiently implemented as a lookup table. The neglected processes and simplifications in this approach are discussed at length in Paper I. It is worth emphasizing here that a different choice of heating and cooling prescriptions can give very different results, in some cases suppressing the unstable region almost entirely (see Wolfire et al. 1995, and their Fig 4 in particular). The prescriptions used here are appropriate for the column density of the initial diffuse atomic cloud in our simulations.

## 4 RESULTS AND DISCUSSION

The evolution of the cloud and the properties of the structure formed across the cloud complex are discussed in this section. In particular, time-variation of properties and derived statistics as well as time-snapshots of slices, projections and isosurface plots reveal these properties. Plotting mechanisms within the MG code are used as well as the visualisation software VisIt (VisIt Collaboration 2012).

### 4.1 The dynamic evolution of the cloud

Fig. 3 provides an overview of the evolution of the cloud, from when the first condensations cause steep density increases at  $t=23$  Myrs to the gravitational contraction of the cloud complex as a whole, on a time-scale of the 50 Myr free-fall time. Strikingly evident from this figure is the formation of obvious filaments, existing with high densities over  $100 \text{ cm}^{-3}$  for more than 10 Myrs. These filaments connect the clumps that are condensing from the unstable medium at the highest density locations. Over time, the clumps grow in size and mass and as the volume of the cloud complex contracts under gravity, effectively absorb the filamentary network that connected them. This is precisely the accepted picture of star formation outlined in the introduction to this paper. Here, this state has evolved naturally from a diffuse stationary initial condition, under only the influence of thermal instability and self-gravity. Of particular importance in this resulting structure are the apparent properties of the filamentary network and we show a column density projection of the structure at  $t=27$  Myrs in Fig. 4. The projection reveals the filaments have a consistent width of 0.002 to 0.006 in scaled units, equivalent to 0.1 to 0.3 pc in physical units. This is in good agreement with the observed range of filamentary widths (Panopoulou et al. 2017) and the debated characteristic width of filaments (Arzoumanian et al. 2018). It is worth repeating here that the resolution of the simulation presented in Fig. 3 is 0.079 pc. The Model 4 simulation goes down to 0.039 pc in high resolution studies of this period of the cloud evolution. The grid resolution is considerably less than the measured width of the filaments in the simulation - they are not forming on the grid scale of these simulations, but instead can only be forming at a natural scale of the thermal instability. Fig. 3 also reveals the long-lasting nature of the filaments - once they have formed, around 25 Myrs into the simulation, they exist for the next 15 Myrs. Measured widths remain approximately constant, although lengths reduce as the clumps approach one another during the gravitational collapse of the whole cloud. There is no evidence in this hydrodynamic simulation of striation-like structure perpendicular to the filaments. This is in agreement with the fact that striations are thought to arise from the effect of magnetic fields (Tritsis & Tassis 2016). We see such magnetically-aligned striations in our MHD simulations (e.g. as can be seen in fig. 3 of Paper IV) and will explore their origins in the follow-on equivalent magnetic paper (in prep.) to this hydrodynamic paper.

The filamentary nature of the cloud in this hydrodynamic simulation came as somewhat of a surprise. Our previous work (Wareing et al. 2016) had revealed filamentary structure in projection of MHD simulations, but no clear indications of filaments in any of the purely HD simulations.

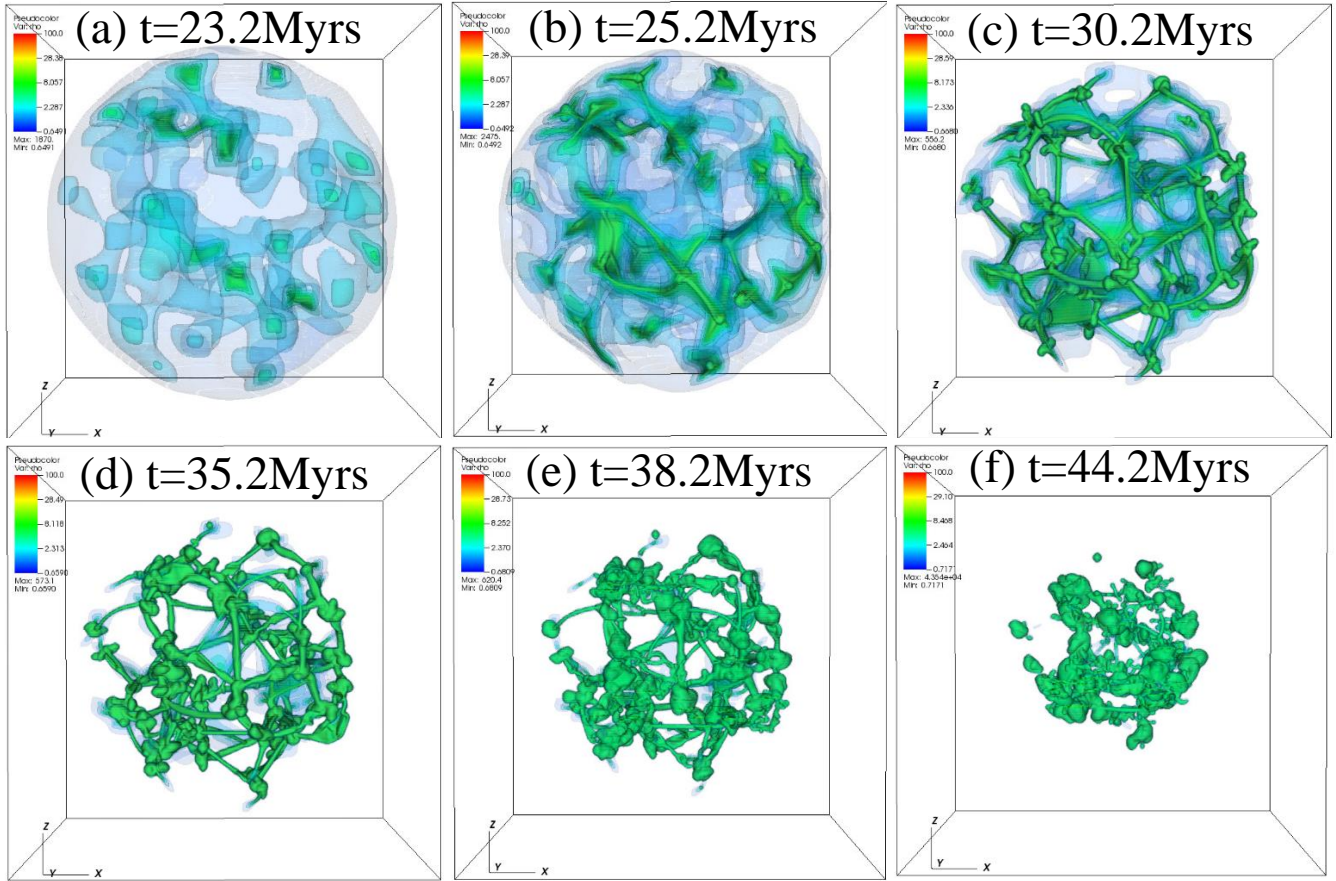


**Figure 3.** Evolution of the diffuse cloud into a complex of clumps shrinking through gravitational collapse. Six time snapshots from Model 3 are shown, in a box with sides of length 50 pc. Each snapshot shows a 3D isosurface rendering of density, with ten isosurfaces shown at density levels ranging linearly up to  $n_H = 100 \text{ cm}^{-3}$ . Isosurface opacity increases with density, reaching high opacity by  $n_H = 10 \text{ cm}^{-3}$ , coloured green in the figure. Lower density more translucent isosurfaces are bluer in colour, indicating the extent of unstable material ( $1 < n_H < 10 \text{ cm}^{-3}$ ). The isosurfaces have been created from Silo datafiles using the Vislt toolkit. Movie and Silo format raw data files are available from <https://doi.org/10.5518/483> (for review purposes see <http://archive.researchdata.leeds.ac.uk/470/>).

That previous work had a base level resolution of 0.29 pc, at least four times lower than that shown in Fig. 3 and comparable to the largest filamentary widths measured from Model 3. Any filaments in earlier HD work should have been at the very limit of detection. Even so, reexamination of the hydrodynamic simulations presented in Paper I reveals that early in their evolution, the numerous clumps forming across the cloud have a tendency to be elongated toward each other. Isosurface rendering has shown this nature more clearly than column density projections shown in Paper I, which are uniformly clumpy. The existence of elongated structure, even at the grid-scale in these early simulations, lends credibility to their convincing detection at the higher resolutions employed here.

It is now prudent to ask if the size-scale of these filaments has any foundation in theoretical examinations of the thermal instability. Aota, Inoue & Aikawa (2013) performed one-dimensional hydrodynamical simulations with detailed heating, cooling and chemical processes, including thermal conduction, to examine the thermal stability of shocked gas in cold neutral medium and molecular clouds. They found characteristic wavelengths of the thermal instability, the perturbation of which can grow within the cooling timescale,

ranged up to 0.1 pc in both the cold neutral medium and in molecular clouds. It is also natural that structure should grow on the acoustic length scale, defined as the sound speed multiplied by the cooling time. Examination of the simulations reveal that the acoustic length scale in the stable dense, cold medium of the filaments is approximately 0.1 pc. The acoustic lengthscale of the warm stable medium surrounding the dense cold structure is approximately 5 pc, not dissimilar to the length scale which separates the clumps from each other and the characteristic length scale which separates sheets in the MHD simulations (see Papers I and II). A reconsideration of the physical length scales associated with the thermal instability is studied in light of new mathematical methods elsewhere (Falle, Wareing & Pittard 2018), further supporting these results.

During the early evolution of the cloud, the over-dense regions present in Fig. 1 increase in density, and then stretch into sheets before becoming filaments, whilst a clump grows at their centre. Examination of the pressure distribution in Fig. 1 illuminates some reasons for this evolution. The regions of higher density correspond to regions of lower pressure, hence the flow of material from high to low pressure increases the density further and pushes the region into cold,

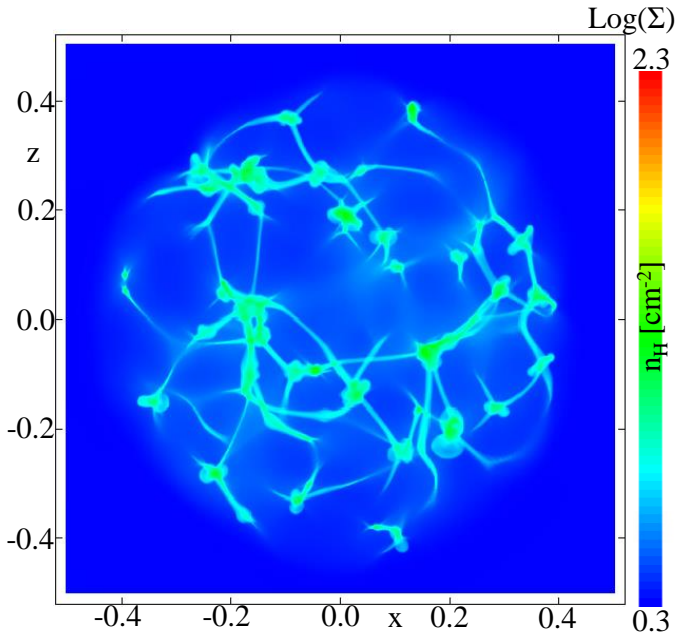


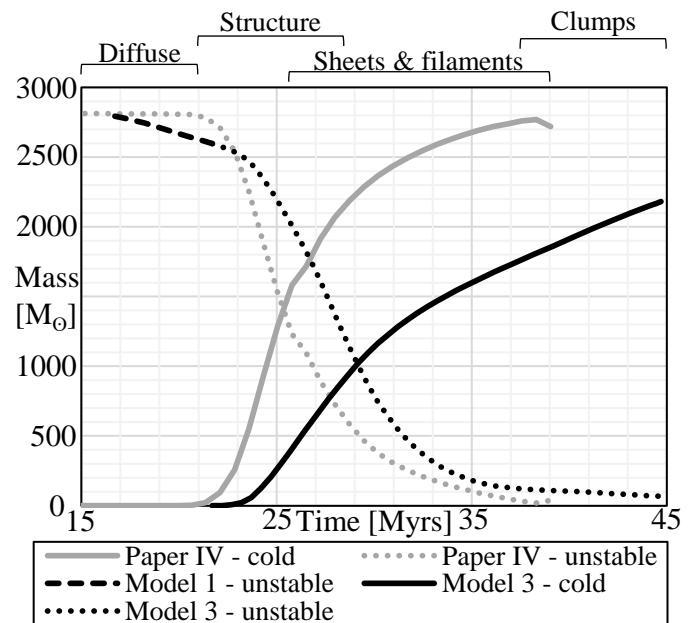
**Figure 4.** Column density, obtained by collapsing the datacube of density along the  $y$  axis, at  $t=27$  Myrs from the Model 3 simulation. The unit of distance is 50 pc. Raw data is available from <https://doi.org/10.5518/483> (for review purposes see <http://archive.researchdata.leeds.ac.uk/470/>).

dense stability. Reducing density at the high pressure locations, as a consequence of material flowing away from these regions, stabilises tenuous low-density warm material. This is analogous to the formation of a foam under phase transition, where the condensed liquid exists in an interconnected filamentary network with bubbles of gas - bench-top X-ray tomography of a monodispersed liquid foam has revealed a strikingly similar structure (Meagher et al. 2011) to that which is produced here and shown in Fig. 3.

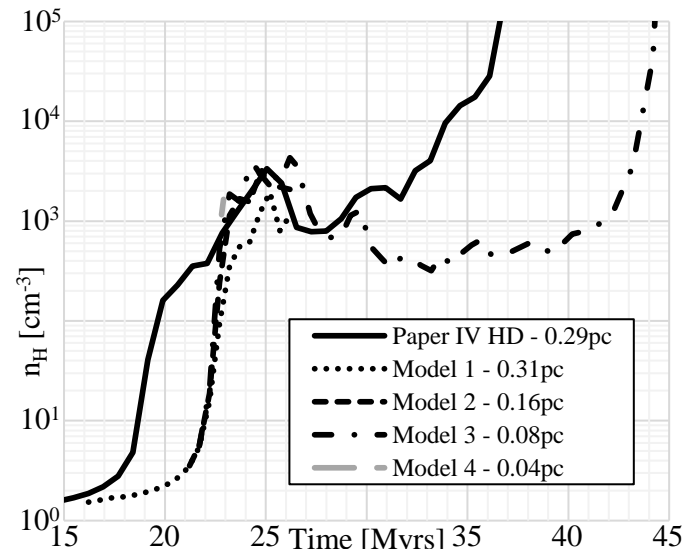
#### 4.2 Evolving properties of the cloud

Fig. 5 shows the mass distribution between phases during the evolution of the cloud, for a subset of the time evolution (the first 15 Myrs of the evolution are not shown as nothing varies). The filamentary network that develops is characteristic of the transitional phase as the simulation evolves the unstable diffuse material into stable states. By the time most of the unstable material has disappeared from the cloud, so have the filaments, absorbed into the individual cold clumps of the collapsing cloud complex. These individual clumps have much higher densities and hence have the potential to collapse under gravity and form stars on shorter timescales than the whole cloud complex.

The variation of maximum density with time is shown in Fig 6, for the same subset of the time evolution. The time indicated on the horizontal axis is that elapsed since the start of the Paper IV HD simulation; the first 15 Myrs are similarly not shown as the maximum density is close to the initial density in the diffuse atomic cloud. The black solid line indicates the trend of maximum density from the Paper IV HD simulation. The steep rise from 18 Myrs is due to condensations close to the edge of the cloud that



**Figure 5.** Evolution of the mass distribution between phases in the domain, with indications of the dominant structure at that time above the line graph. Raw data is available from <https://doi.org/10.5518/483> (for review purposes see <http://archive.researchdata.leeds.ac.uk/470/>).



**Figure 6.** Evolution of the maximum density in the domain. The faster formation of dense clumps in the Paper IV HD simulations is due to the compression at the outer surface of the cloud, which results from our choice of initial conditions (see main text). Raw data is available from <https://doi.org/10.5518/483> (for review purposes see <http://archive.researchdata.leeds.ac.uk/470/>).

have been influenced by the pressure difference caused by the reducing average pressure across the cloud compared to that of the surrounding medium. Whilst these may or may not be representative of reality, in this work the study of thermal instability and gravity is under examination, hence the isolation of the central region of the Paper IV HD cloud. This is also the reason for the *reduction* in the maximum

density present in the domain at the initialisation of the Model 1 simulation.

The maximum densities in the Model 1-4 simulations are representative of structure solely generated from the thermal instability. These simulations show that thermal instability triggers a steep rise in density around 22 Myrs, as the filamentary network forms. During this steep rise, the Model 2 and Model 3 simulations are both launched in order to ensure resolution of later structure; the branching of the simulations is earlier than the maximum density peaks as launching at peak density risks loss of unresolved structure. By 23 Myrs, the maximum density in the Paper IV HD simulation is back in agreement with the maximum densities present in the Model 2 and 3 simulations. The maximum density in the Paper IV simulation is now representative of TI-driven structure in the inner cloud, rather than condensations at the edge of the cloud that originated from the pressure difference between cloud and surroundings. By 25 Myrs, the maximum density in all simulations is in agreement and reaches  $n_{\text{H}} \approx 3000 \text{ cm}^{-3}$ . A detailed inspection of this behaviour (Model 4 simulation) indicated that it *does not* lead to gravitationally bound clumps that may subsequently form stars. Inspection of the velocity field around these structures reveals velocities on the order of a few  $\text{km s}^{-1}$  that are non-convergent, resulting from flow of thermally-stable material from warm, tenuous to cold, dense conditions. Kinetic energy dominates and as a result, these structures break apart on relatively short timescales compared to their free-fall times. The long duration of the relatively high maximum density in Fig 6 from 24 to 27 Myrs is indicative of the period over which the long-lived filamentary structures form and evolve in the cloud. It is not the peak density of individual clumps that may collapse under the effect of gravity. The Model 3 simulation resolves the peak in maximum densities into several separate peaks for this reason.

The importance of correctly identifying this period of dynamically-dominated structure in any simulations cannot be over-emphasized. Dynamical and non-equilibrium effects have been shown to be important for cloud evolution (Goicoechea et al. 2016). Mechanisms for forming star particles could mis-identify these regions of high density, as they meet conditions for inward flow, potential minimum and Jeans instability. Depending on the frame of reference selected for calculating energies, the balance between kinetic, gravitational and thermal energy can also be misleading, an issue that has also been noted in observations (Ballesteros-Parades et al. 2018). Followed carefully at high resolution, they do not collapse under their own self-gravity.

The original Paper IV HD simulation contained sharp unresolved structures at this time and did not resolve multiple dynamic peaks around 25 Myrs, but did capture the transience of this period, reducing back to lower densities in the cloud until the true collapse of quiescent TI-structure begins around 29 Myrs. The resolved Model 3 simulation captures the behaviour beyond this point showing that longer-lasting filamentary structure forms with densities on the order of several hundred per cubic centimetre. By 40 Myrs or so individual clumps have gathered enough mass to begin to collapse under the influence of gravity. This is against the background of the infall towards the deep central potential well at the centre of the domain. There is therefore a long

period of time (up to 10 Myrs from  $t=28$  Myrs) where the cloud consists of quiescent high density clumps connected by lower density filaments that have not collapsed under gravity. These clumps have size scales on the order of a few pc and are therefore not diffuse microstructure in the ISM (Stanimirović & Zweibel 2018), but do resemble pressure confined clumps noted as a pre-requisite for star formation (Kainulainen et al. 2011). Whilst we do not track the formation of molecules, the timescale here is not dissimilar to the  $\sim 10$  Myr time scale of cloud formation recently derived for formation of molecular hydrogen in an isolated dark cloud (Zuo et al. 2018).

### 4.3 Model 3 cloud at $t=44$ Myrs

The appearance of the cloud as a whole at  $t=44$  Myrs is shown in Figs. 7 and 8. This is the time at which nearly all of the unstable material has stabilised and can be considered the thermal end-state of the cloud. The remaining unstable material is in thin layers surrounding the clumps. Few filaments remain. In the unrealistic scenario that stars do not form, the future of the cloud is collapse under gravity on the free-fall timescale of the cloud. The question is whether individual clumps can or are collapsing on shorter time scales. Slices of density, pressure, temperature and potential through the simulation domain show the clumpy nature of the cloud complex, as well as the fact that only the most massive clumps have increased central pressures at this time. The temperature slice shows both temperature on the colour scale and vectors of total velocity projected onto this plane. The uniformity of the warm stable surroundings is immediately apparent - there is effectively very little variation across this intra-clump medium, even though the flow field is complex. The velocity vectors show there are inflows towards the individual clumps apparent on this plane, as well as the overall infall towards the centre of the most massive clump. The depth of the potential well, as well as the previously noted smooth nature of the distribution is apparent from the slice through potential. These slices through the domain do not show any filamentary structures. At this time, they are now rare, having been absorbed into clumps, or dissipated along their length into chains of smaller clumps. Fig. 8 shows projections of column density in the three axial directions and a density isosurface of the Model 3 simulation, revealing the few remaining filaments. In particular, in the upper right of panel (a), the break-up of a filament into a series of clumps along its length appears to be occurring at this late time.

### 4.4 Model 3 clump analysis

It is now meaningful to identify and analyse massive clumps in the simulation. The FellWalker clump identification algorithm (Berry 2015) has been implemented into MG in order to do this. Berry described FellWalker as a watershed algorithm that segments multi-dimensional data above a pre-set background level into a set of disjoint clumps, each containing a significant peak. It is equivalent in purpose to the CLUMPFIND algorithm (Williams, de Geus & Blitz 1994), but unlike CLUMPFIND, FellWalker is based on a gradient-tracing scheme which uses *all* the available data, ‘walking’

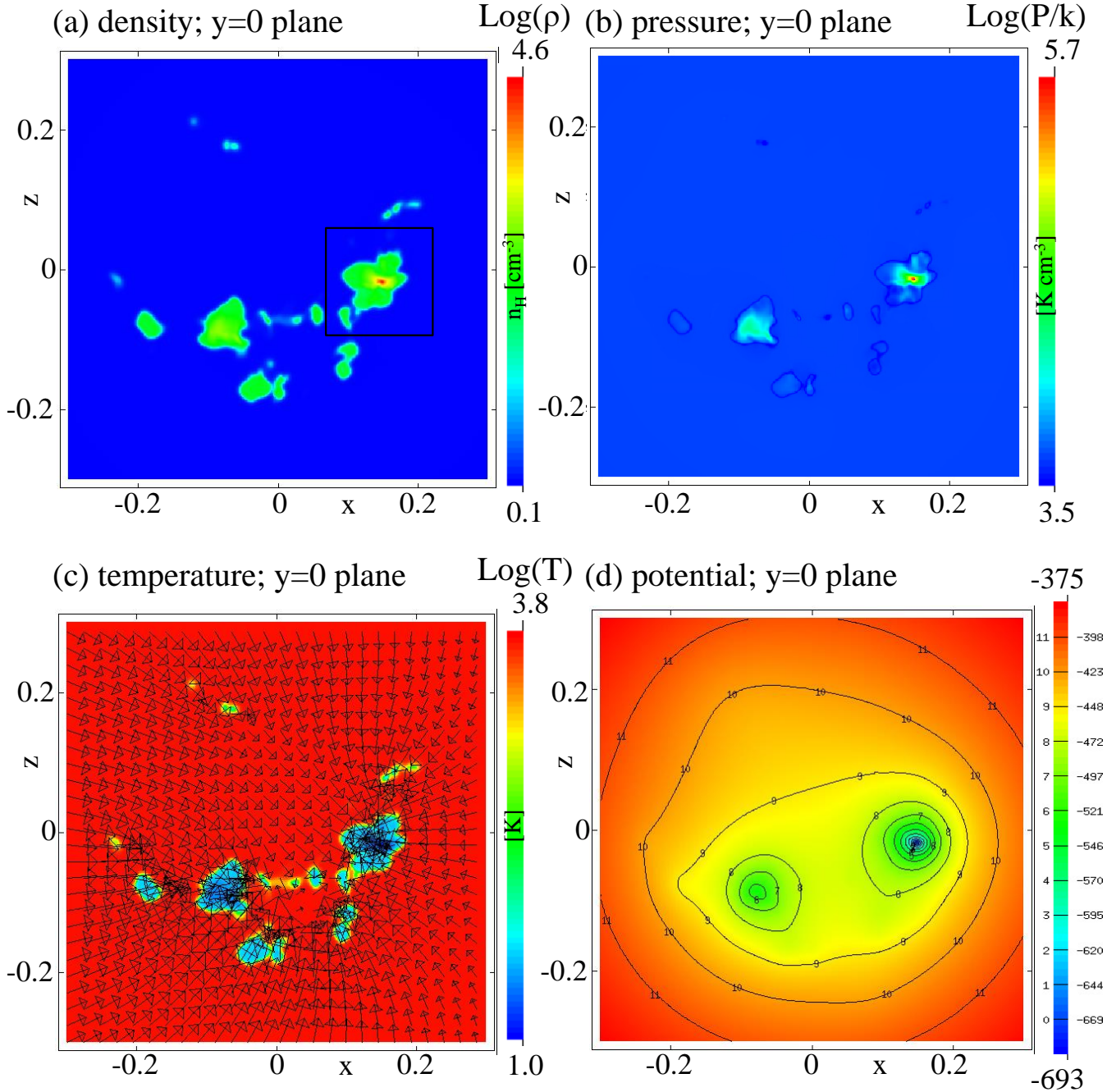


**Figure 7.** The evolved simulation, showing a slice through the domain at  $y=0.11328$  through the densest clump in the grid. Shown are (a) density, (b) pressure, (c) temperature and (d) gravitational potential of the Model 3 simulation at  $t=44$  Myr. Vectors of velocity, scaled on the largest magnitude in the slice of  $2.5 \text{ km s}^{-1}$ , are shown in panel (c). The box in panel (a) indicates the volume, centred on the most massive clump, resimulated later at higher resolution. The unit of distance is 50 pc. Raw data is available from <https://doi.org/10.5518/483> (for review purposes see <http://archive.researchdata.leeds.ac.uk/470/>).

from each datapoint according to the steepest gradient to the peak associated with that gradient. Berry performed comparisons with CLUMPFIND and showed that the results produced by FellWalker are less dependent on specific parameter settings than are those of CLUMPFIND.

Whilst Berry designed FellWalker to identify significant peaks in density, here FellWalker has been implemented to identify significant wells in gravitational potential. The gravitational potential has a significantly smoother distribution

than the mass distribution and hence makes an excellent choice for identifying clumps directly from the simulation without any parameterised smoothing step. After implementation, the algorithm was thoroughly tested with simple 2- and 3-dimensional potential distributions to establish confidence in the performance and understand the optimum grid configuration for usage. In order to achieve the best results, we applied FellWalker to the potential projected onto the finest grid level. The potential is sufficiently smooth for the

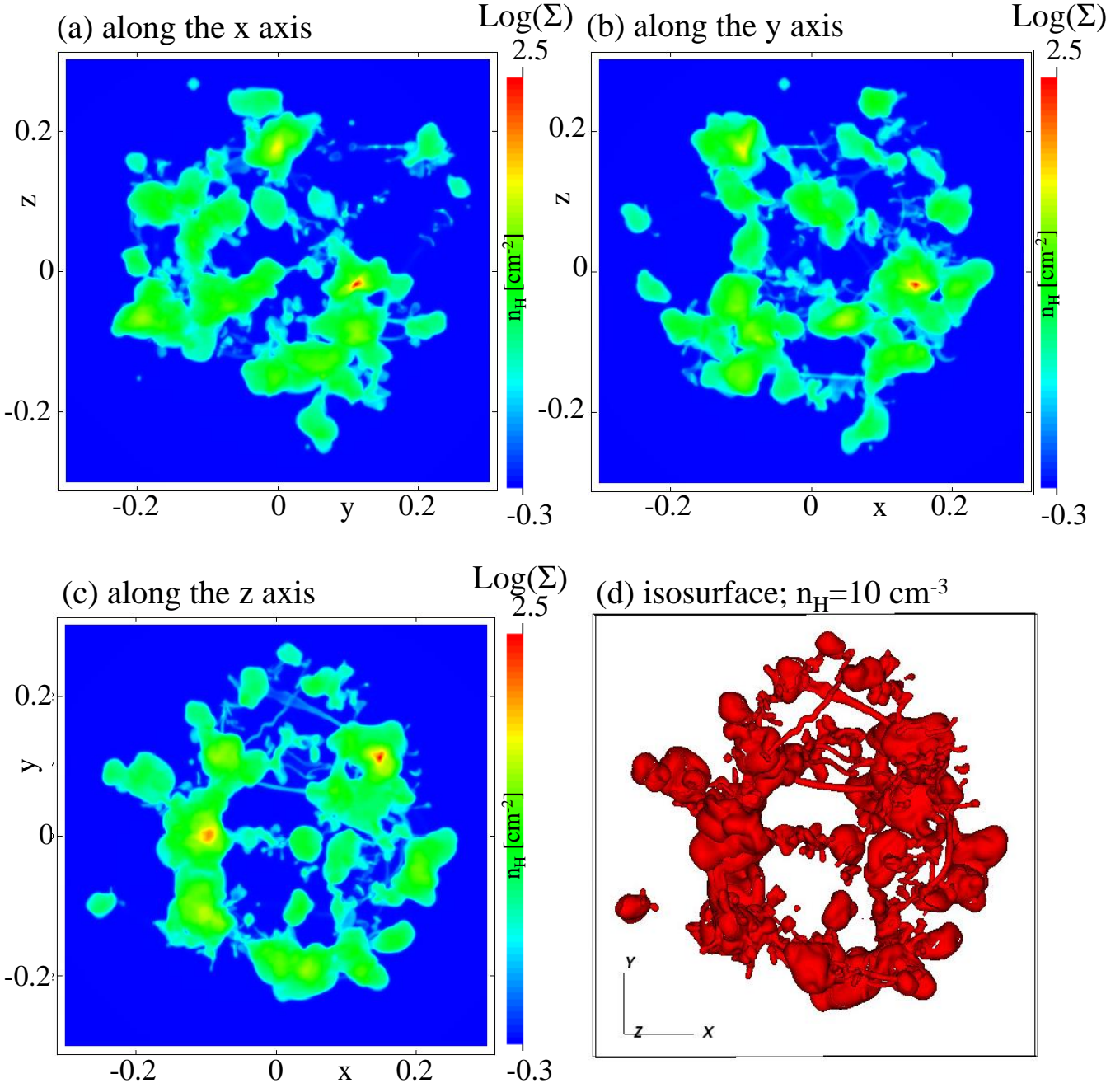


**Figure 8.** Projections of column density in the three axial directions and an isosurface of density, rotated to match the projection along the  $z$  axis for side-by-side comparison, of the Model 3 simulation at  $t=44$  Myrs as in the previous figures. The unit of distance is 50 pc. Raw data is available from <https://doi.org/10.5518/483> (for review purposes see <http://archive.researchdata.leeds.ac.uk/470/>).

projection from coarser grids to be smooth enough for FellWalker.

Applying FellWalker to the Model 3 simulation snapshot at  $t=44$  Myrs, the algorithm detects 21 individual clumps with masses greater than  $20 M_{\odot}$ . This particular time is the time at which the highest density in the simulation, in the centre of the most massive clump, reaches the limit of the resolution. It should be noted that this most massive clump is not at the centre of the simulation. The term ‘clump’ is used by choice in order to achieve clarity from the diffuse initial cloud condition and the cloud com-

plex that the combination of these clumps forms. Bergin & Tafalla (2007) review the properties of clumps based on Loren (1989) and Williams, de Geus & Blitz (1994): mass  $50-500 M_{\odot}$ ; size  $0.3-3 \text{ pc}$ ; mean density  $10^3-10^4 \text{ cm}^{-3}$ ; velocity extent  $0.3-3 \text{ km s}^{-1}$ ; crossing time 1 Myr; and, gas temperature 10-20 K. Properties of the 21 massive clumps identified in the Model 3 simulation are shown in Table 1. The range of mass, maximum density, size scale and velocity fit the description of Bergin & Tafalla very well. In each clump, the majority ( $> 75\%$ ) of the mass is in the cold phase. Minimum temperatures, which occur in the inner regions of each

**Table 1.** Properties of the 21 clumps with more than  $20 M_{\odot}$  identified by the FellWalker algorithm, at  $t=44$  Myr in the Model 3 simulation. Snapshots of slices through the clumps are available from <https://doi.org/10.5518/483> (for review purposes see <http://archive.researchdata.leeds.ac.uk/470/>).

	$M_{total}$ [ $M_{\odot}$ ]	$M_{warm}$ [ $M_{\odot}$ ]	$M_{unstable}$ [ $M_{\odot}$ ]	$M_{cold}$ [ $M_{\odot}$ ]	$\rho_{max}$ $n_H$ [cm $^{-3}$ ]	$T_{min}$ [K]	Scale [pc]	$v_{max}$ [km s $^{-1}$ ]	$v_{min}$ [km s $^{-1}$ ]	Notes
A	2.37e2	5.39e1	3.19e0	1.78e2	4.62e2	30.5	3.5	2.2	0.11	Spheroidal, extended arms
B	2.64e2	2.36e1	4.10e0	2.37e2	9.92e2	21.5	4.0	2.8	0.31	Prolate spheroid
C	2.71e2	4.49e1	4.25e0	2.22e2	7.76e2	22.9	4.0	2.4	0.12	Pyramidal
D	3.54e2	5.65e1	6.49e0	2.92e2	1.46e4	10.6	4.0	2.5	0.17	Multiple lobes
E	7.27e1	1.05e1	1.01e0	6.12e1	4.16e2	31.3	2.5	1.9	0.03	Spheroidal
F	1.08e2	1.55e1	1.01e0	9.12e1	4.32e2	28.8	4.0	2.6	0.06	Double sphere merger
G	1.77e2	1.94e1	2.65e0	1.55e2	3.31e2	32.7	4.0	2.1	0.04	Peanut
H	2.65e1	2.01e0	3.19e-1	2.42e1	1.54e2	32.4	2.4	2.5	0.03	Clump on a filament?
I	7.57e1	5.88e0	1.06e0	6.88e1	1.94e2	33.4	3.0	2.2	0.18	Results of a merger?
J	3.13e1	2.59e0	2.93e-1	2.84e1	2.16e2	32.0	3.0	3.2	0.08	Co-flowing clumps
K	1.04e2	5.10e0	1.14e0	9.76e1	4.18e2	26.9	2.5	1.8	0.03	Isolated. Spherical
L	2.37e1	1.02e0	3.28e-1	2.23e1	2.83e2	31.1	1.0	2.5	0.01	Tadpole, 2.5 pc elongated tail
M	6.83e1	1.16e1	1.07e0	5.57e1	4.95e2	26.1	3.0	2.7	0.03	Elongated. Chain?
N	9.14e1	8.50e0	1.42e0	8.15e1	3.33e2	29.3	3.0	2.4	0.33	Spheroidal, linked filament?
O	4.85e1	8.63e0	1.28e0	3.87e1	2.34e2	29.9	3.0	1.7	0.02	Spheroidal - 2 filaments
P	6.84e1	2.20e1	1.66e0	4.47e1	1.89e2	33.1	3.0	1.9	0.07	Large tadpole
Q	6.63e1	5.19e0	9.80e-1	6.01e1	2.86e2	32.1	4.0	1.8	0.03	Sph. Off-centre max rho
R	2.96e2	3.19e1	2.76e0	2.62e2	3.25e3	16.9	5.0	2.4	0.13	Multiple lobes - subclumps?
S	7.25e1	7.70e0	1.00e0	6.38e1	3.92e2	27.4	5.0	2.5	0.02	Double merger
T	3.57e1	1.53e0	7.64e-1	3.34e1	2.06e2	33.0	3.0	2.3	0.03	Prolate spheroid
U	3.36e1	3.72e-1	3.91e-1	3.28e1	2.03e2	33.6	2.5	2.7	0.15	Spheroidal, sub-clumps

clump where the lowest velocity also occurs, are typically slightly higher than Bergin & Tafalla's review; only the two most massive clumps, D and R, are colder than 20 K in their core. It is worth noting that maximum density and minima of temperature and velocity are all co-located in these cold ( $< 100$  K) inner regions of each clump, but often not at the centre of mass of the clump, reflecting the complex evolution that has produced these clumps. The maximum velocity is usually found at the edge of the clump, which is well-defined by a sharp gradient in temperature. Material there is falling into the clump whilst rapidly cooling and decelerating through the phase change - these are dynamic rather than stationary accreting objects. They are not simply cold clumps stabilising out of quiescent unstable surroundings. The surroundings are in fact in the warm stable phase and the only unstable region is across the sharply defined edge of the clump, hence the "unstable" mass (defined as that in the unstable region of Fig 2, with densities between  $n_H=1.0$  and  $10.0$  cm $^{-3}$ ) is a small fraction of the total clump mass.

The appearance of the clumps is varied, as noted in Table 1. Very few are isolated and spherical, reflective of the fact that they have absorbed filaments and smaller clumps. What Table 1 only partially alludes to, is the remnants of filamentary interconnecting structures between clumps. This is present at  $t=44$  Myrs as smaller condensations where a filament has dissipated along its length, extended wings stretching away from the clumps where filaments are being absorbed and the existence of isolated small clump-like structures. These small structures have masses on the order of a few solar masses or less and have shallow potential wells, if any discernible effect on the gravitational potential. In time, the isolated small structures may grow, or merge into existing clumps, as all are falling toward the centre of the cloud complex. At this time in the Model 3 simulation, there are no discernible sheet-like cloud collisions. The sub-

sonic velocities in the simulations here do not lead to shock-compressed thin structures.

The maximum and minimum velocities in Table 1 are not reflective of the velocity dispersion of the individual clumps. The maximum velocity reflects the typical velocity of the infalling material at the edge of the clump. Further analysis has shown that the minimum velocity is typical of the velocity dispersion of the cold material in the clump, on the order of 0.2-0.5 km s $^{-1}$  or less. This is at most trans-sonic in cold regions of the clump, given the temperature range up to 100 K. At the edges of the clump, the velocity of the infalling material is subsonic in the warm stable medium, but becomes trans- and even mildly supersonic as material cools at the edge of the clump. This would appear to be in-line with observations of sonic velocities around clumps, which must dissipate for the clump to eventually collapse under the effect of gravity, converting kinetic energy into thermal and gravitational energy - the potential well deepens whilst the pressure at the centre of the clump rises. The clumps in Table 1 display clear evidence of the relationship between increasing density and deepening individual potential wells, even set against the background of the potential of the cloud complex as a whole. Interestingly, on the smaller scale of cores, Ballesteros-Parades et al. (2018) find the extension of this from clumps to cores - the observed energy budget of cores in recent surveys is consistent with their non-thermal motions being driven by their self-gravity and in the process of dynamical collapse. Furthermore, Micic et al. (2013) study the influence of cooling functions on the formation of molecular clouds and find, in agreement with previous models, that the majority of clumps are not self-gravitating, suggesting that some large-scale collapse of the cloud may be required in order to produce gravitationally unstable clumps and hence stars. We see that effect here and now go on to study an individual clump in detail, followed

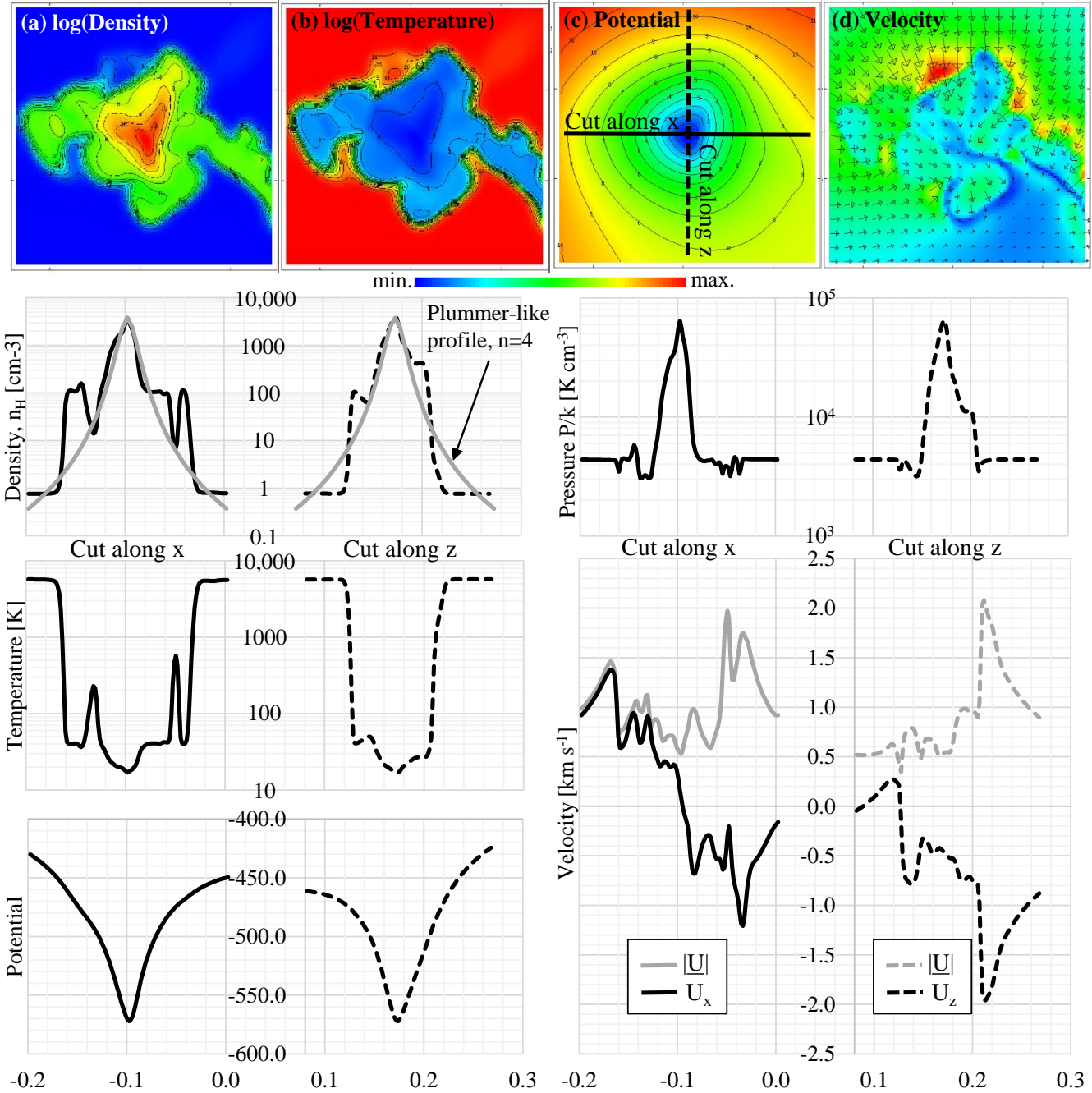


**Figure 9.** Properties of Clump R from the Model 3 simulation at  $t=44$  Myr. The unit of distance is 50 pc. Raw data is available from <https://doi.org/10.5518/483> (for review purposes see <http://archive.researchdata.leeds.ac.uk/470/>).

by study of the final collapse of the most massive clump identified in Table 1.

#### 4.5 Study of an individual clump from Model 3

Turning to examine an individual clump in more detail, Figure 9 shows slices and profile cuts through Clump R, the second most massive clump in the Model 3 Simulation at  $t=44$  Myrs. The slices and profiles are cut through the position of the deepest potential of the clump, at  $(-0.0977, 0.00078, 0.174)$ . The centre of mass of the clump is slightly

offset at  $(-0.103, 0.00209, 0.181)$ , equivalent to 0.44 pc between centre of potential and centre of mass - further reflecting the non-symmetric, non-spherical nature of this clump, 5 pc in length along its major axis. The cut along  $x$  reveals multiple peaks in density, with corresponding complex velocity structure, due to the absorption of the filamentary network and merger with other clumps. It is interesting at this point to compare the density distribution to previous assumptions about clumps. Clearly the clump does not have a uniform density distribution. It does, around the central peak, have a Plummer-like density distribution, indicated in

the figure by the agreement between the data (black line) and theoretical profile (grey line). In the negative  $x$  direction, this agreement stretches over two orders of magnitude in density - on a linear  $y$ -axis scale, the agreement appears very close. The comparison here is with the classic Plummer-like profile introduced by Whitworth & Ward-Thompson (2001), with the observationally confined power-law index of 4, rather than the true Plummer sphere with index of 5. The fit takes a central density of  $n_H = 3780 \text{ cm}^{-3}$  from the data and a minimal central flat radius of 0.01 ( $\approx 0.5 \text{ pc}$ ). The temperature plot serves to illustrate the sharply defined edge of the clump, where the temperature ranges quickly from the lower inner temperatures below 100 K, to the high temperature ( $> 5000 \text{ K}$ ) of the warm stable surroundings. Peaks in the inner temperature profiles revealed by the  $x$  cut, which correspond to troughs in density, again show evidence for merger with earlier structure in the cloud.

The distribution of the potential, shown in panel (c) of Fig 9 is remarkable for its smoothness compared to the complex structure apparent in density. In the context of simulated molecular clouds, gravitational potential is clearly useful for identification of distinct clumps with structure-finding tools such as FellWalker or CLUMPFIND. The magnitude of total velocity is shown in Fig. 9(d), along with vectors indicating the direction of velocity, projected onto this plane. Whilst some information is lost in this projection, the figure makes it apparent that the highest density, coldest regions of the clump correspond to the lowest velocities (deepest blues) inside the clump. The complexity of the velocity field is also apparent, indicating accelerating inflow from above the clump. Note that velocity on this slice is presented in the frame of reference of the entire simulation domain, rather than corrected for the motion of the centre of mass of the clump towards the centre of the slowly collapsing cloud complex. Clearly, velocity reduces as material flows, under the action of the thermal instability, across the phase boundary from warm tenuous to cold dense material. In turn, the dispersion of velocity reduces across this boundary. Of key importance in Fig. 9 are the cuts though pressure across the clump. The central pressure is an order of magnitude greater than the equilibrium pressure in the warm surroundings, clearly indicating gravitational collapse. The conditions are close to thermal equilibrium, with pressure at the centre a few percent higher than the corresponding thermal equilibrium pressure for that density. The central density is not in dynamical equilibrium and is still rising as the clump continues to collapse.

In Fig. 10 we show the snapshot power spectra of velocity and density both for the cloud complex as a whole and for Clump R at  $t=44 \text{ Myrs}$ . The power spectra have been calculated from the magnitude of the complete velocity vector ( $v_x, v_y, v_z$ ) and the density. There is no projection or smoothing of the velocity vector into two components on a plane (as has been shown to affect velocity power spectra by Medina et al. 2014). Power spectra have been calculated using a simple IDL routine which performs the Fourier Transform and bins the square of the 3D transform into wavenumbers to obtain the 1D power spectra. The validity of this method has been checked by generating density structures in 1D, 2D and 3D. These structures have been generated using single wavenumber sine waves with varying wavenumbers and combinations of these sine waves with multiple com-

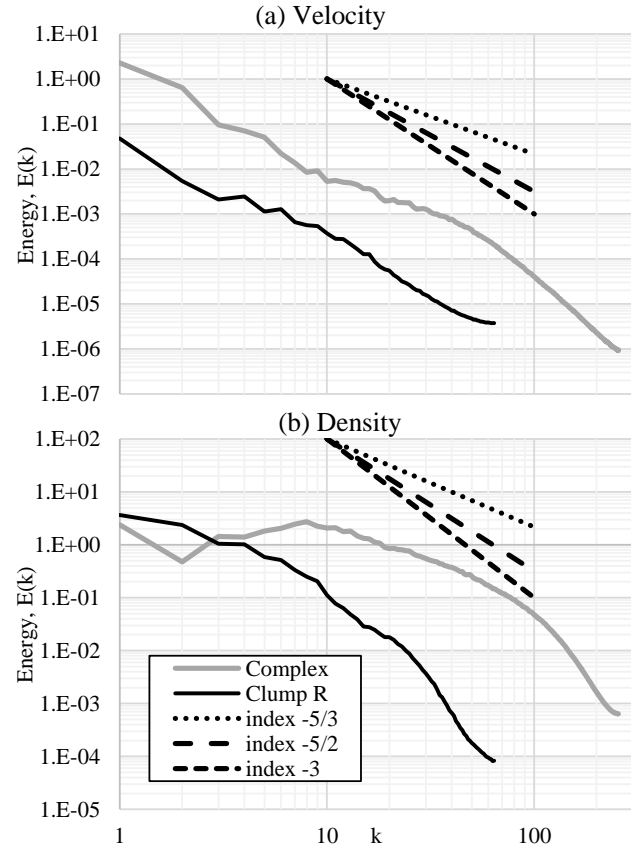


**Figure 10.** Instantaneous power spectra of a) velocity and b) density for the cloud as a whole and for clump R at  $t=44 \text{ Myrs}$ . Raw data is available from <https://doi.org/10.5518/483> (for review purposes see <http://archive.researchdata.leeds.ac.uk/470/>).

ponent wavenumbers to ensure the power spectra analysis returns the correct wavenumber(s) that was(were) used to generate the density structure in the first place.

Clear from the power spectra of velocity is that both the cloud complex and Clump R display an inertial range (region in wavenumber with slope of constant gradient) greater than one order of magnitude. The cube encompassing the cloud complex transformed for this analysis was 40 pc on a side. Between wavenumbers 3 and 30 (or physical scales from 13 pc down to 1 pc), the spectral index is close to the Kolmogorov  $-5/3$  spectrum generally observed in turbulence. This is in good agreement with observationally-derived velocity power spectra, for example an index of  $-1.81 \pm 0.10$  derived by Padoan et al. (2006) for the Perseus molecular cloud complex. At  $k = 30$  there is a break in the spectrum, to an index steeper (less than) than  $-3$  implying rapidly reducing kinetic energy with decreasing physical size scale. The validation tests showed that single precision numerical noise generated an index of  $-5$  when a pure, single wavenumber sinewave was used to generate 3D input data, tending to indicate therefore there is still some power at these scales as the spectrum is not as steep as  $-5$ . Calculation of power spectrum at earlier times shows that before 23 Myrs, the index of the spectrum is steeper than  $-3$ , but this rapidly softens as to  $-5/2$  high density structure emerges around 25 Myrs. From  $t=30 \text{ Myrs}$  onwards, the velocity power spec-

trum of the cloud complex has reached a steady state and is as shown in Fig. 10. The velocity power spectra of Clump R is an order of magnitude less powerful than that observed in the cloud complex as a whole. The cube encompassing Clump R for the Fourier Transform was 10 pc on a side and power spectra of Clump R are hence reduced by a factor of  $4^3$  in order to allow direct comparisons between cloud and Clump spectra. Again the velocity power spectra has two inertial ranges over which the spectral indices are approximately constant, this time with a break between the two at  $k = 10$  - notably the same physical scale of 1 pc. At length-scales longer than 1 pc (lower wavenumbers), the inertial range is again  $-5/3$  - indicating consistent sampling of the same thermal instability flow in the warm stable medium in this smaller box. At shorter length-scales, typically inside the clump, the index is approximately  $-3$ , not dissimilar to that simulated by others on that scale and below (Medina et al. 2014).

It is remarkable that a simulation that started out as a stationary diffuse cloud and that generates large-scale ordered flows, displays a long-lasting turbulence-like  $-5/3$  spectrum on an inertial range across one decade of wavenumber, *even though there is no fully developed turbulence in this simulation and there was no driving scale in the initial condition*. What the simulation has generated is flow containing a “hierarchy of small-scale irregularities superimposed on larger-scale more systematic motions” – very much the definition of Larson-like turbulence (Larson 1981, and “1. Introduction” therein for the source of this quote). This result also makes it difficult to determine the nature of clumps, as what may appear turbulent is actually a signature of complex infall velocities. Previous authors have noted that clumps with clear signatures of infall are statistically indistinguishable from clumps with no such signatures (Traficante et al. 2018). The same authors noted that the observed non-thermal (i.e. supersonic) motions are not necessarily ascribed to turbulence acting to sustain gravity, but they may be due to the gravitational collapse at clump scales – precisely what we see here. Given the extensive nature of the warm neutral medium, this results suggests that this index of  $-5/3$  should extend to larger spatial scales than considered here - i.e. there is no physical reason for an inertial range limiting upper physical scale. It should be noted that fully developed turbulence, even in astrophysical scenarios, displays an inertial range over many orders of magnitude in  $k$ , for example in the magnetic fields of neutron stars (Wareing & Hollerbach 2009, 2010). Galactic-scale simulations have found that the correlation scale of the large-scale random flows, calculated from the velocity auto-correlation function, is on the order of 100 pc (Gent et al. 2013). This may or may not lead to a break in power spectra at this scale, but is larger than the scales considered here, lending support to our finding of structured, or correlated, flows on scales shorter than 100 pc. Further work is required to answer questions over how the large-scale turbulent nature of galaxies may be converted to correlated flows below the correlation length. The lower physical scale limit of the turbulence-like inertial range is however a resolved physical characteristic of the models – specifically, the scale of the cold condensations produced by thermal instability. It should not shift to smaller physical size (higher wavenumber) with the use of greater resolution. Given the nature of the energy change

across the phase boundary, with increasing infall velocity on the scale of a few  $\text{km s}^{-1}$  on the warm side of the boundary, rapidly decreasing to an order of magnitude lower velocities on the cold side of the boundary, it would be natural to call the  $\sim$ few pc scale of these cold dense clumps the “dissipative limit” of the turbulent velocity spectrum of the warm neutral medium.

The power spectra of density in the cloud complex peaks at  $k = 8$ . As noted previously, the size of the cube used for the Fourier Transform is 40 pc on a side so this is equivalent to 5 pc and in expected agreement with the 5 pc scale of the dense clumps in the cloud. There is some sign of an inertial range between  $k = 8$  and  $k = 40$  with an index around  $-5/3$ , reflective of the substructure in the clumps. Given there is structure throughout the cloud on the scale of 1 to 5 pc as shown in Figs. 7 and 8, this seems reasonable. At  $k > 40$ , there is a steepening of the power spectra, indicating relatively less smaller-scale structure. Calculation of density power spectrum at earlier times shows that before 23 Myrs, the spectrum is far less powerful and weakly peaked at large  $k$  on the small scale ( $\sim$ 1 pc) of the growing inhomogeneities (as well as an expected strong peak at the scale of the entire cloud complex). As structure grows in the simulation, the density power spectrum rapidly rises and steepens, although takes a longer period to display a steady state spectral index than the velocity power spectrum. From 35 Myrs onwards, the density power spectrum is in agreement with the snapshot spectrum shown here in Fig. 10, although rising in power (shifting directly upwards in the figure) as densities increase in the clumps. Clump R displays a power spectra of density in agreement with this, with structure on the order a few pc (up to  $k = 4$ ) before a steepening power spectra. If Clump R were spherical with radius 5 pc, we would expect a peak at  $k = 2$  from this 10 pc box analysis, but as clearly shown in Fig. 9, the clump is anything but spherical. There is no inertial range, but the spectral index steepens from approximately  $-5/2$ , indicating that this clump, where self-gravity has taken over from the effect of the thermal instability, is not dissimilar to those simulated elsewhere (Medina et al. 2014). There are also similarities with observations of the Perseus molecular cloud, where multi-phase density power spectra with indices of  $-5/2$  and steeper are derived (Pingel et al. 2018).

Again, it is worth highlighting that the power spectra resulting from these simulations which start from a stationary initial condition, are not dissimilar from those that start from turbulent initial conditions, nor dissimilar to observed power spectra. There is also no evidence for the 0.29 pc resolution scale of the initial simulation in Paper IV – the spectra are smooth across  $k$  of 138 for the cloud complex and  $k$  of 34 for the Clump R spectra). If anything can be considered a ‘driving scale’ in these simulations, it is that 0.29 pc scale upon which the initial density inhomogeneities are introduced at  $t = 0$ . There is no evidence that this scale has dominated our simulations and it is very different to the 5 pc acoustic length scale of the warm stable medium that seems to be observed defining clump-scales here and sheet separation scales in the magnetic case (see Papers I and IV).

Further study is required to determine whether the use of power spectra can meaningfully discern between models of star formation, but these results indicate power spectra are a blunt tool for understanding the formation of molecular

clouds. The results also cast doubt on any justification for the injection of driven turbulence in numerical models of molecular clouds, since it is apparent that our simulations naturally produce long-lasting turbulence-like power spectra from stationary initial conditions.

#### 4.6 Final collapse

The most massive clump, Clump D, has been extracted and resimulated at even higher resolution (0.016 pc on the finest AMR level) in order to examine the collapse of the clump and confirm that it is gravitationally bound and Jeans unstable. On a short time scale of approximately 100,000 years, from  $t=44$  Myrs to  $t=44.1$  Myrs, the density in the clump rises steeply up to  $n_H = 3.5 \times 10^6 \text{ cm}^{-3}$ . 91% of the mass in the clump, equivalent to approximately  $250 M_\odot$ , is in the cold phase. The unstable envelope around the clump contains little more than one solar mass of material. The central pressure in the clump has risen to two orders of magnitude greater than the average pressure of the warm stable surroundings. An energy analysis of the simulated data reveals that the clump is strongly gravitationally bound - the clump has three times more gravitational energy than the sum of kinetic and thermal energy, making it also Jeans unstable. The apparent nature of the clump is very similar to that shown in Fig. 9, albeit with a far greater peak density. A Plummer-like profile is a good fit, but again substructure in the clump means there are large variations in different radial directions outward from the peak density.

In combination with the simulations presented earlier, we have conclusively demonstrated that thermally unstable diffuse material can evolve cold and dense structure which can be strongly influenced by gravity. This can lead to the eventual collapse of such structure under gravity, without the need to include any other physics or factors, e.g. pressure waves, shocks or collisions, although clearly these play a role which can now be elucidated in future work. Remarkably, in the purely hydrodynamic case, the natural evolution of the diffuse unstable cloud produces a distribution of cold, dense clumps connected by long-lived filaments that would appear to have a characteristic size scale of 0.1 to 0.3 pc.

### 5 CONCLUSIONS

In this work, we set out to determine by the use of hydrodynamic simulation whether a molecular cloud structure evolved from diffuse, thermally unstable medium could ever lead to gravitationally collapsing structure, without the influence of any other physics (e.g. turbulence) or external disturbance (pressure wave, shock or collision).

Our previous work, at lower resolution of 0.29 pc or greater, had revealed that clumpy clouds form in the hydrodynamic case and corrugated sheet-like clouds, that in projection appear filamentary, form in the magnetic case. Neither set of previous simulations conclusively demonstrated gravitational collapse within such models of molecular clouds.

The suite of high-resolution simulations carried out here, with typically 0.078 pc resolution, but up to 0.016 pc resolution, have now conclusively demonstrated that thermal instability in a diffuse medium alone can generate cold

and dense enough structure to allow self-gravity to take over and conclude the star formation process. The total time scale for this to happen is on the order of 40 Myrs, although the structure would only be considered a molecular cloud for the previous 15 Myrs. The final gravitational collapse sees density increase by 3 orders of magnitude on very short time scales of  $10^5$  years.

We have noted the following:-

- (i) Diffuse thermally unstable material evolves into a stable network of cold dense clumps multiply-connected by filaments, immersed in warm tenuous material.
- (ii) The filaments have a narrow width distribution of 0.1 to 0.3 pc.
- (iii) During the early evolution of the cloud complex, high densities in the filaments and proto-clumps caused by thermal instability driven flow can be mis-leading, in terms of applying automatic star particle injection routines. Convergent flow, energy analysis and gravitational potential conditions can all be satisfied, but accurate investigation reveals this to be a transient dynamical phase in the formation of the cloud complex, not gravitational collapse.
- (iv) Application of the FellWalker (Berry 2015) algorithm identifies 21 massive ( $> 20 M_\odot$ ) clumps that have formed in this  $3,000 M_\odot$  region of cloud.
- (v) The clumps formed have a size-scale of 5 pc or less, masses up to  $300 M_\odot$ , internal temperatures of 10-30 K and internal velocity dispersions of  $0.5 \text{ km s}^{-1}$  or less. These physical characteristics are in agreement with the definition of clumps presented by Bergin & Tafalla (2007) and density distributions can be fitted by a Plummer-like profile (Whitworth & Ward-Thompson 2001).
- (vi) In agreement with previous models (see Micic et al. 2013, and references therein) the majority of clumps are not initially collapsing. The most massive clump has been investigated at 0.016 pc and does collapse under gravity, increasing its central density by 3 orders of magnitude on a time scale of 100,000 years.
- (vii) Velocity power spectra of the cloud complex as a whole and an individual massive clump show spectral indices which are turbulence-like ( $-5/3$ ) over a short inertial range (approximately one decade of wavenumber), even though the initial diffuse condition was stationary. This is indicative of large-scale flow with a hierarchy of small-scale structure, very much as predicted by Larson (1981). The wavenumber of the break-point in the spectrum corresponds to the 5 pc size-scale of individual clumps.
- (viii) Power spectra of velocity and density are not dissimilar to simulations that employ turbulent initial conditions implying that 1D power spectra may not offer a meaningful tool to discern between models of star formation.
- (ix) The most massive clumps eventually undergo runaway gravitational collapse with analysis determining that they are truly gravitationally bound and Jeans unstable.

Immediate future work will consider the effect of magnetic fields in this scenario, applying the same high resolution to MHD simulations (which have been run along side this suite of simulations) and looking for gravitational collapse in the magnetic case, as well as explanations for the origins of striations (Tritsis & Tassis 2016), disconnections along filaments resulting in ‘integral-shapes’ (Stutz, Gonzalez-Lobos & Gould 2018) and the formation of

strongly distorted magnetic fields, e.g. hour-glass field morphologies (Pattle et al. 2017). Other work will study the effect of various feedback mechanisms in this cloud complex, introducing a robust star-particle formation technique, sampling a realistic initial mass function in order to determine the star formation rate of this cloud complex.

## ACKNOWLEDGMENTS

We acknowledge support from the Science and Technology Facilities Council (STFC, Research Grant ST/P00041X/1). The calculations herein were performed on the DiRAC 1 Facility at Leeds jointly funded by STFC, the Large Facilities Capital Fund of BIS and the University of Leeds and on other facilities at the University of Leeds. Data presented herein is available from <http://doi.org/10.5518/483> (for review purposes see <http://archive.researchdata.leeds.ac.uk/470/>). We thank David Hughes at Leeds for the provision of IDL scripts which formed the basis of the power spectra analysis presented in this work. VisIt (VisIt Collaboration 2012) is supported by the Department of Energy with funding from the Advanced Simulation and Computing Program and the Scientific Discovery through Advanced Computing Program.

## REFERENCES

André P., Di Francesco J., Ward-Thompson D., Inutsuka S.-I., Pudritz R. E., Pineda J. E., 2014, in Beuther H., Klessen R. S., Dullemond C. P., Henning T., eds, *Protostars and Planets VI*. University of Arizona Press, Tucson, 914. p. 27, preprint (arXiv:1312.6232)

Aota T., Inoue T., Aikawa Y., 2013, *ApJ*, 775, 26

Arzoumanian D. et al., 2018, *A&A* accepted, arXiv:1810.00721

Ballasteros-Paredes J., Vázquez-Semadini E., Palau A., Klessen R. S., 2018, *MNRAS*, 479, 2112

Bastien P., 1983, *A&A*, 119, 109

Bergin E. A., Tafalla M., 2007, *ARA&A*, 45, 339

Berry D. S., 2015, *Astronomy and Computing*, 10, 22

Beuther H., Linz H., Henning T., eds, 2008, *ASP Conf. Ser.* Vol. 387. *Massive Star Formation: Observations Confront Theory*. Astron. Soc. Pac., San Francisco

Birk G. T., 2000, *Physics of Plasmas*, 7, 3811

Bruhweiler F. C., Freire Ferrero R., Bourdin M. O., Gull T. R., 2010, *ApJ*, 719, 1872

Falle S. A. E. G., 1991, *MNRAS*, 250, 581

Falle S. A. E. G., 2005, *Proceedings of the Chicago Workshop on Adaptive Mesh Refinement Methods*, Springer Lecture Notes in Computational Science and Engineering (Springer, New York, USA), 41, 235

Falle S. A. E. G., Wareing C. J., Pittard J. M., 2018, *MNRAS*, submitted

Hubber D. A., Falle S. A. E. G., Goodwin S. P., 2013, *MNRAS*, 432, 711

Federrath C., Roman-Duval J., Klessen R. S., Schmidt W., Mac Low M.-M., 2010, *A&A*, 512, id.A81

Field G. B., 1965, *ApJ*, 142, 531

Fukue T., Kamaya H., 2007, *ApJ*, 669, 363

Gatto A., et al. 2015, *MNRAS*, 449, 1057

Gent F. A., Shukurov A., Fletcher A., Sarson G. R., Mancini M. J., 2013, *MNRAS*, 432, 1396

Girichidis P., et al. 2015, *MNRAS*, accepted, arXiv: 1508.06646

Gnat O., Ferland G. J., 2012, *ApJS*, 199, article id. 20

Godunov S. K., 1959, *Mat. Sbornik*, 47, 271

Goicoechea J. R. et al., 2016, *Nature*, 537, 209

Gómez G. C., Vázquez-Semadini E., 2014, *ApJ*, 791, article id. 124

Gray W. J., Scannapieco E., 2011, *ApJ*, 733, 88

Harper-Clark E., Murray N., 2009, *ApJ*, 693, 1696

Heitsch F., Stone J. M., Hartmann L. W., 2009, *ApJ*, 695, 248

Hennebelle P., Audit E., 2007, *A&A*, 465, 431

Hennebelle P., Audit E., Miville-Deschénes M.-A., 2007, *A&A*, 465, 445

Hennebelle P., Banerjee R., Vázquez-Semadini E., Klessen R. S., Audit E., 2008, *A&A*, 486, L43

Hennebelle P., André P., 2013, *A&A*, 560, id.A68

Heyer M. H., Brunt C. M., 2004, *ApJ*, 615, L45

Inoue T., Inutsuka S.-I., 2012, *ApJ*, 759, article id. 35

Kainulainen J., Beuther H., Banerjee R., Federrath C., Henning T., 2011, *A&A*, 530, id.A64

Kawamura A. et al., 2009, *ApJS*, 184, 1

Kirk H., Klassen M., Pudritz R., Pillsworth S., 2015, *ApJ*, 802, article id. 75

Koenig X. P., Leisawitz D. T., Benford D. J., Rebull L. M., Padgett D. L., Assef R. J., 2012, *ApJ*, 744, 130

Körtgen B., Seifried D., Banerjee R., Vázquez-Semadini E., Zamora-Avilés M., 2016, *MNRAS*, 459, 3460

Koyama H., Inutsuka S.-I., 2000, *ApJ*, 532, 980

Koyama H., Inutsuka S.-I., 2002, *ApJ*, 564, L97

Krumholz M. R., Burkhardt B., 2016, *MNRAS*, 458, 1671

Krumholz M. R., Matzner C. D., 2009, *ApJ*, 703, 1352

Kuriganov A., Tadmor E., 2000, *J. Co. Ph.*, 160, 241

Larson R. B., 1981, *MNRAS*, 194, 809

Li Z.-Y., Wang P., Abel T., Nakamura F., 2010, *ApJ*, 720, L26

Lim A. J., Falle S. A. E. G., Hartquist T. W., 2005, *ApJ*, 632, L91

Loren R. B., 1989, *ApJ*, 338, 925

Mac Low M.-M., Klessen R. S., 2004, *Reviews of Modern Physics*, 76, 125

Meagher A. J., Mukherjee M., Weaire D., Hutzler S., Banhart J., Garcia-Moreno F., 2011, *Soft Matter*, 7, 9881

Medina S.-N. X., Arthur S. J., Henney W. J., Mellema G., Gazol A., 2014, *MNRAS*, 445, 1797

Micic M., Glover S. C. O., Banerjee R., Klessen R. S., 2013, *MNRAS*, 432, 626

Moeckel N., Burkert A., 2015, *ApJ*, 807, article id. 67

Nejad-Asghar M., Ghanbari J., 2003, *MNRAS*, 345, 1323

Offner S. S. R., Arce H. G., 2015, *ApJ*, 811, article id. 146

Ostriker E. C., McKee C. F., Leroy A. K., 2010, *ApJ*, 721, 975

Padoan P., Juvela M., Goodman A. A., Nordlund Å., 2001, *ApJ*, 553, 227

Padoan P., Juvela M., Kritsuk A., Norman M. L., 2006, *ApJ*, 653, L125

Panopoulou G. V., Psaradaki I., Skalidis R., Tassis K., Andrews J. J., 2017, *MNRAS*, 466, 2529

Parker E. N., 1953, *ApJ*, 117, 431

Pattle K., et al. 2017, *ApJ*, 846, article id. 122

Pingel N. M., Lee M.-Y., Burkhardt B., Stanimirović S., 2018, ApJ, 856, 136

Porter D., Pouquet A., Woodward P. R., 1994, Phys. Fluids, 6, 2133

Rogers H., Pittard J. M., 2013, MNRAS, 431, 1337

Rogers H., Pittard J. M., 2014, MNRAS, 441, 964

Shadmehri M., 2009, MNRAS, 397, 1521

Smith R., Glover S. C. O., Klessen R. S., 2014, MNRAS, 445, 2900

Solomon P. M., Rivolo A. R., Barrett J., Yahil A., 1987, ApJ, 319, 730

Stanimirović S., Zweibel E. G., 2019, ARAA, 56, 489

Stutz A., Gonzalez-Lobos V. I., Gould A., MNRAS *submitted*. arXiv:1807.11496

Stiele H., Lesch H., Heitsch F., 2006, MNRAS, 372, 862

Traficante A., Duarte-Cabral A., Elia D., Fuller G. A., Merello M., Molinari S., Peretto N., Schisano E., Di Giorgio A., 2018, MNRAS, 477, 2220

Tritsis A., Tassis K., 2016, MNRAS, 462, 3602

Truelove J. K., Klein R., McKee C. F., Holliman J. H. II, Howell L. H., Greenough J. A., 1997, ApJL, 489, L179

Van Loo S., Falle S. A. E. G., Hartquist T. W., 2010, MNRAS, 406, 1260

Van Loo S., Tan J. C., Falle S. A. E. G., 2015, ApJ, 800, article id. L11

Vázquez-Semadini E., 1994, ApJ, 423, 681

Vázquez-Semadini E., Gómez G.C., Jappsen A. J., Ballasteros-Paredes J., González R. F., Klessen R. S., 2007, ApJ, 657, 870

VisIt Collaboration, 2012, in “High Performance Visualisation – Enabling Extreme-Scale Scientific Insight”, pp. 357-372

Walch S. K., Naab T., 2015, MNRAS, 451, 2757

Walch S. K., et al. 2015, MNRAS, 454, 238

Wareing C. J., Hollerbach R., 2009, Physics of Plasmas, 16, 042307

Wareing C. J., Hollerbach R., 2010, Journal of Plasma Physics, 76, 117

Wareing C. J., Pittard J. M., Falle S. A. E. G., Van Loo S., 2016, MNRAS, 459, 1803; Paper I

Wareing C. J., Pittard J. M., Falle S. A. E. G., 2017a, MNRAS, 465, 2757; Paper II

Wareing C. J., Pittard J. M., Falle S. A. E. G., 2017b, MNRAS, 470, 2283; Paper III

Wareing C. J., Pittard J. M., Wright N. J., Falle S. A. E. G., 2018, MNRAS, 475, 3598; Paper IV

Whitworth A. P., Ward-Thompson D., 2001, ApJ, 547, 317

Williams J. P., de Geus E. J., Blitz L., 1994, ApJ, 428, 693

Wolfire M. G., Hollenbach D., McKee C. F., Tielens A. G. G. M., Bakes E. L. O., 1995, ApJ, 443, 152

Zuo P., Li D., Peek J. E. G., Chang Q., Zhang X., Chapman N., Goldsmith P. F., Zhang Z.-Y., 2018, ApJ, 867, 13